

2D Metastable-Phase Hafnium Oxide Triggers Hydrogen Spillover for Boosting Hydrogen Production

**Qun Wang, Jinxin Chen, Shiya Chen, Dingyanyan Zhou, Yutong Du, Yujin Ji,*
Yutian Xiong, Jia Ke, Wenxiang Zhu, Yue Wang, Dongdong Gao, Wei-Hsiang Huang,
Chih-Wen Pao, Yang Sun, Youyong Li, Mingwang Shao, Zhiwei Hu, Xiaoqing Huang,*
and Qi Shao***

Hydrogen (H) manipulation plays a significantly important role in many important applications, in which the occurrence of hydrogen spillover generally shows substrate-dependent behavior. It therefore remains an open question about how to trigger the hydrogen spillover on the substrates that are generally hydrogen spillover forbidden. Here a new metastable-phase 2D edge-sharing oxide: six-hexagonal phase-hafnium oxide (Hex-HfO₂, space group: P6₃mc (186)) with the coordination number of six is demonstrated, which serves as an ideal platform for activating efficient hydrogen spillover after loading Ru nanoclusters (Ru/Hex-HfO₂). For a stark comparison, the hydrogen spillover is strongly forbidden when using stable monoclinic phase HfO₂ (M-HfO₂, space group: P2₁/c (14), coordination number: seven) as the substrate. When applied in an acidic hydrogen evolution reaction (HER), Ru/Hex-HfO₂ exhibits a low overpotential of 8 mV at 10 mA cm⁻² and a high Ru utilization activity of 14.37 A mg_{Ru}⁻¹ at 30 mV. Detailed mechanism reveals the positive H adsorption free energy on Hex-HfO₂, indicating that H is more likely to spillover on Hex-HfO₂. Furthermore, the strong interaction between Ru and Hex-HfO₂ optimizes the desorption of hydrogen intermediate, thus facilitating the surface H spillover. The discovery provides new guidance for developing metastable-phase oxide substrates for advanced catalysis.

friendly.^[1–3] Generally, hydrogen regulation involves multiple intermediate steps, including adsorption, dissociation, reaction, and desorption.^[1,4,5] All of these steps may be influenced by factors such as the catalyst structure, active sites, and reaction conditions.^[6–8] Therefore, it is both vital and challenging to decouple and control the hydrogen-mediated reaction pathways.

Hydrogen spillover has emerged as one of the most promising technologies for regulating the behavior of hydrogen species.^[9,10] It is a widespread interfacial phenomenon involving the migration of equivalent amounts of H atoms from metal nanoparticles to support and participates in the catalytic conversion process of substances adsorbed on a carrier.^[11–13] Since the initial discovery of the hydrogen spillover effect (HSPE) on Pt/WO₃ catalyst by Boudart in 1964, it has sparked significant research interest in hydrogen storage and catalysis.^[14,15] Pursuing a suitable substrate is the key factor in triggering hydrogen spillover^[16,17] since the adjustable structure and properties allow for the

customization of designs tailored to specific reaction requirements.^[18] However, HSPE shows structure-dependent behavior, where the substrate with a specific composition is generally forbidden.^[19] Therefore, it has tremendous potential to

1. Introduction

Hydrogen (H) is a pivotal element in catalytic processes, owing to its exceptional energy density, renewability and environmentally

Q. Wang, Y. Du, Y. Xiong, J. Ke, Y. Wang, Q. Shao
College of Chemistry
Chemical Engineering and Materials Science
Soochow University
Suzhou, Jiangsu 215123, China
E-mail: qshao@suda.edu.cn

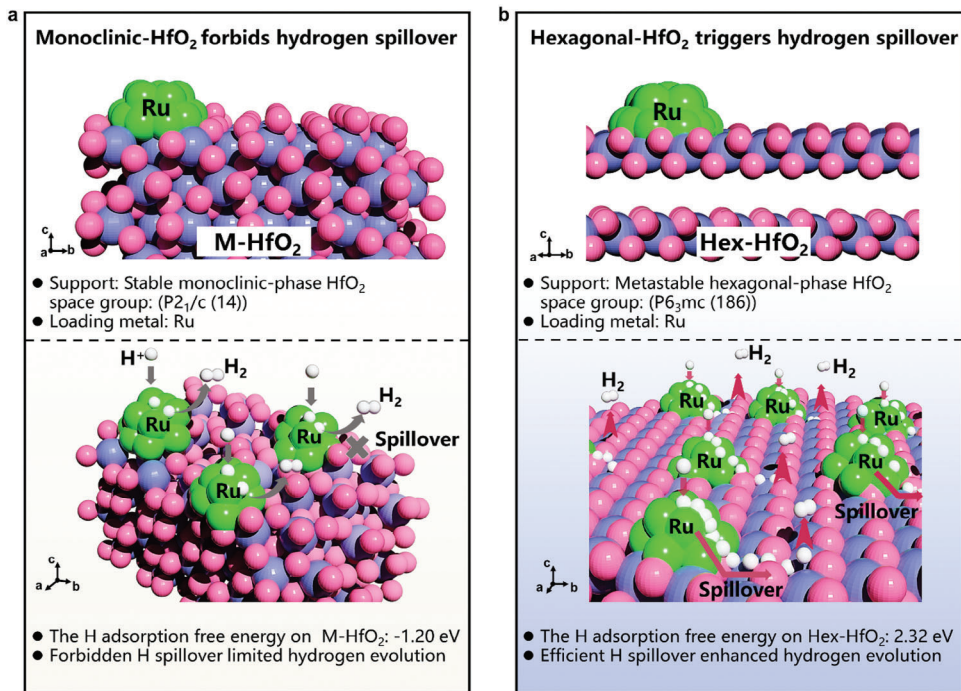
Q. Wang, J. Chen, D. Zhou, Y. Ji, W. Zhu, D. Gao, Y. Li, M. Shao
Institute of Functional Nano & Soft Materials (FUNSOM)
Soochow University
Suzhou, Jiangsu 215123, China
E-mail: yji@suda.edu.cn

S. Chen, Y. Sun
Department of Physics
Xiamen University
Xiamen, Fujian 361005, China
W.-H. Huang, C.-W. Pao
National Synchrotron Radiation Research Center
101 Hsin-Ann Road, Hsinchu 30076, Taiwan

Z. Hu
Max Planck Institute for Chemical Physics of Solids
Notnitzer Strasse 40, 01187 Dresden, Germany
X. Huang
State Key Laboratory of Physical Chemistry of Solid Surfaces
College of Chemistry and Chemical Engineering
Xiamen University
Xiamen, Fujian 361005, China
E-mail: hxq006@xmu.edu.cn

 The ORCID identification number(s) for the author(s) of this article can be found under <https://doi.org/10.1002/adma.202415978>

DOI: 10.1002/adma.202415978



Scheme 1. Schematic illustration of hydrogen spillover on different substrates. a) Monoclinic phase HfO_2 (M-HfO_2) forbids hydrogen spillover effect. b) Hexagonal phase HfO_2 (Hex-HfO_2) triggers hydrogen spillover effect. Green balls represent Ru atoms, blue balls represent Hf atoms and red balls represent O atoms.

regulate the phase structure of substrate, transforming it from spillover-forbidden to spillover-activated one.^[20,21] A metastable phase refers to a state that is not the most thermodynamically stable but is relatively stable under certain conditions. Compared to stable-phase materials, metastable-phase materials typically have higher Gibbs free energy, different structures, bond formation, and reaction intermediate rupture. Consequently, metastable-phase materials become a promising candidate for solving this challenge.^[22–25] However, how to design a phase-engineered substrate to trigger hydrogen spillover has barely been proposed.

The stable phase hafnium oxide (HfO_2) belongs to the monoclinic phase (M-HfO_2) with a space group of $\text{P}2_1/\text{c}$ (14), which is a typical hydrogen spillover-forbidden material^[26] (Scheme 1a). Therefore, it is considered as a representative candidate to investigate the effect of phase engineering regulation on hydrogen spillover. Inspired by all these possibilities, we reported a new 2D layered metastable-phase oxide: six-hexagonal phase-hafnium oxide (Hex-HfO_2 , space group: $\text{P}6_3\text{mc}$ (186)), synthesized by the molten-alkali mechanochemical method. Surprisingly, when dispersing Ru nanoclusters uniformly on Hex-HfO_2 , we observed the obvious occurrence of hydrogen spillover phenomenon on Ru/Hex-HfO_2 (Scheme 1b). Thanks to the significant hydrogen spillover effect, Ru/Hex-HfO_2 showed high acidic hydrogen evolution reaction (HER) activity with an overpotential of 8 mV at a current density of 10 mA cm^{-2} , a low Tafel slope of 24 mV dec^{-1} , and an ultrahigh mass activity of $14.37 \text{ A mg}_{\text{Ru}}^{-1}$ at the overpotential of 30 mV. Density functional theory (DFT) calculations revealed the H adsorption free energy of Hex-HfO_2 is 2.32 eV, compared to -1.20 eV for M-HfO_2 , which triggers the H spillover behavior on Ru/Hex-HfO_2 . The discovery will provide a novel in-

sight for developing phase-engineered hydrogen spillover-based catalysts.

2. Results and Discussion

Hex-HfO_2 was synthesized via a molten-alkali mechanochemical method. In a typical experiment, HfCl_4 and KOH were mixed and thoroughly ground in the corundum mortar and the mixture was heated by a mechano-thermal method. The final product of Hex-HfO_2 is white (Figure S1a, Supporting Information). Scanning electron microscopy (SEM) and transmission electron microscopy (TEM) were applied to characterize the morphology of Hex-HfO_2 , revealing its 2D hexagonal nanosheet morphology (Figure 1c; Figure S1b, Supporting Information). The crystal structure of Hex-HfO_2 was first revealed by the X-ray diffraction (XRD) pattern, as shown in Figure 1a,b. Hex-HfO_2 exhibits completely different diffraction peaks from monoclinic phase HfO_2 (JCPDS 34–0104). The crystal parameter along the c-direction can be determined to be $c = 30.608 \text{ \AA}$. In addition, energy dispersive X-ray spectroscopy (EDX) results reflect that Hf and O are uniformly distributed in Hex-HfO_2 and the atomic ratio of Hf to O is $\approx 1:2$ (Figure 1d; Figure S2, Supporting Information). The high-resolution transmission electron microscopy (HRTEM) image shown in Figure 1e displays the fringe patterns showing the presence of the (10-10) and (0-110) planes of Hex-HfO_2 . The aberration-corrected dark-field scanning transmission electron microscopy (STEM-ADF) image shown in Figure 1f clearly reveals the nanosheet structure, in which the hexagonal lattice of the Hex-HfO_2 layer can be observed. The well-resolved atomic structure displays that the crystal parameters could be

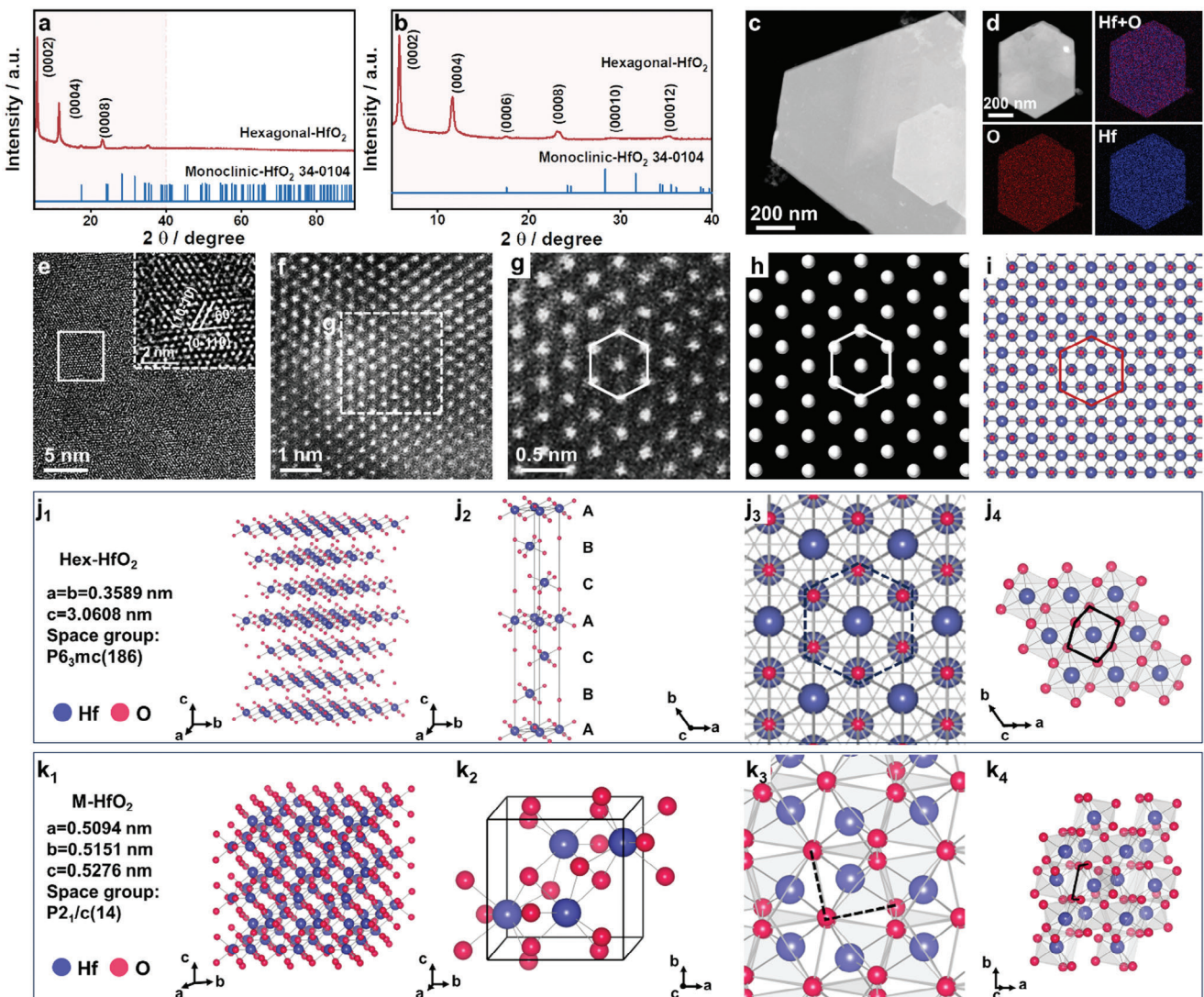


Figure 1. Crystal structure and morphology characterization of Hex-HfO₂. a) XRD pattern. b) Partial enlargement from (a). c) TEM image. d) STEM and the corresponding elemental mapping images. e) HRTEM image and its partially enlarged view. f) STEM-ADF image. g) High magnification image of the region in (f). h) Simulated STEM-ADF image. i) Atom model. Comparison of crystal structure diagrams of j) Hex-HfO₂ and k) M-HfO₂.

determined as $a = b = 3.589\text{ \AA}$ and one Hf atom is surrounded by six adjacent Hf atoms. The high-magnification image with the corresponding models is shown in Figure 1g–i, respectively, further vividly reveal the structure. Due to the proportionality between the intensity of atomic columns and atomic numbers, a hexagonal pattern of Hf atoms was observed, while the intensity of oxygen columns was too weak to be visible. The selected area electron diffraction (SAED) patterns of Hex-HfO₂ are hexagonal consistent with its hexagonal structure (Figure S3, Supporting Information). Brunauer–Emmett–Teller (BET) adsorption–desorption isotherm reveals that the Hex-HfO₂ nanosheet exhibits a relatively high surface area ($42.06\text{ m}^2\text{ g}^{-1}$), larger than that of M-HfO₂ ($3.57\text{ m}^2\text{ g}^{-1}$) (Figure S4, Supporting Information).

We also explored the synthetic method by changing different synthetic parameters. First of all, the mechanical-thermal

method provides high temperatures and grinding pressure, offering higher energy for the formation of metastable-phase materials.^[27] Only amorphous products can be obtained by directly mixing HfCl₄ and KOH without mechanical grinding (Figure S5, Supporting Information). We investigated the roles of the alkaline environment and temperature in the synthesis process. When using K₂CO₃ and KHCO₃ as precursors, only monoclinic phase hafnium oxide can be obtained (Figure S6, Supporting Information). This indicates the significant role of strong alkaline conditions in the synthesis of metastable-phase materials. At the same time, at temperatures of 300 and 500 °C, only amorphous hafnium oxide can be obtained. When the temperature increased to 1200 °C, potassium hafnate (JCPDS No. 20–0882) was produced (Figure S7, Supporting Information). The thermogravimetric analysis demonstrates that within the temperature range from room temperature to 900 °C, Hex-HfO₂ has no obvious

mass loss, indicating its good thermal stability (Figure S8, Supporting Information). The morphology and crystal structure of Hex-HfO₂ remained unchanged after soaking in water or ethanol (Figure S9a–d, Supporting Information). It can be maintained at room temperature for half a year, indicating excellent chemical stability (Figure S9e,f, Supporting Information).

In order to further compare the structural differences between Hex-HfO₂ and M-HfO₂, M-HfO₂ has also been characterized in detail in Figure S10 (Supporting Information). The XRD peaks could be indexed as monoclinic phase HfO₂ (JCPDS No. 34–0104) (Figure S10b, Supporting Information). SEM and TEM images show the morphology of M-HfO₂ nanoparticles (Figure S10c,d, Supporting Information). The lattice space of 3.15 Å can be assigned to the (-111) crystal plane of M-HfO₂ (Figure S10e, Supporting Information). EDX results reflect that Hf and O are uniformly distributed in M-HfO₂ (Figure S10j–l, Supporting Information). Therefore, we summarize different directional structural models for Hex-HfO₂ and M-HfO₂ in Figure 1j,k, respectively. It can be seen that Hex-HfO₂ exhibits significant differences in the unit cell and coordination connection compared to M-HfO₂. The M-HfO₂ is arranged as the monoclinic phase with the space group of No. 14 (P2₁/c) (Figure 1k). Hf atoms are surrounded by seven oxygen atoms, corresponding to a mixture of seven-edge shared polyhedra and four-corner shared polyhedra in the unit cell.^[26] A stark contrast to M-HfO₂ is that the [HfO₆] octahedra in the hexagonal phase of Hex-HfO₂ are layered stacks with edge-sharing and the coordination number of Hf is six, corresponding to the space group of No. 186 (P6₃mc). In Hex-HfO₂, a single unit consists of six layers of [HfO₆], arranged in an ABCACB stacking sequence (Figure 1j).

The elemental states and electronic structure of Hex-HfO₂ and M-HfO₂ are also compared. As depicted in the X-ray photoelectron spectroscopy (XPS) spectra, Hex-HfO₂ exhibits a positive shift of Hf 4f_{7/2} and Hf 4f_{5/2} peaks (16.8 and 18.4 eV) in comparison with those for M-HfO₂ (16.4 and 18.0 eV), which indicates that Hex-HfO₂ has higher Hf valence state than M-HfO₂ (Figure S11, Supporting Information). The X-ray absorption near-edge structure (XANES) shows that the white-line peak of Hf L-edge for Hex-HfO₂ is higher than that of M-HfO₂, further indicating that the Hf atoms of Hex-HfO₂ show higher oxidation state than M-HfO₂ (Figure 2e). The Fourier transform of extended X-ray absorption fine structure (EXAFS) spectra at the Hf L-edge was conducted to investigate the local coordination environment. As shown in Figure 2f, the EXAFS spectra mainly contain two peaks, the first one corresponds to the nearest Hf–O bond and the second one is the nearest Hf–Hf bond.^[28] The first-shell Hf–O coordination of Hex-HfO₂ is at 1.60 Å, which is not significantly different from M-HfO₂. However, the second-shell Hf–Hf coordination at 2.78 Å of Hex-HfO₂ downshifts compared with that of M-HfO₂ (2.90 Å), which may be attributed to the different polyhedral connection in the monoclinic phase HfO₂ and hexagonal phase HfO₂.^[29] It is worth noting that the intensity of the Hf–Hf peak of Hex-HfO₂ has a lower peak intensity than M-HfO₂, which may be attributed to the varying degrees of distortion in the arrangement structure of cations and the different coordination numbers in different crystal phase structures that lead to multiple scattering events, thus affecting the propagation of signals.^[30,31] The wavelet transform (WT) of EXAFS shows that Hex-HfO₂ exhibits one intensity maximum value for

Hf–O coordination at ≈6.3 Å⁻¹ in k space and ≈2.6 Å in R space, which is larger and smaller than those (≈4.8 Å⁻¹ and 3.0 Å) of M-HfO₂, suggesting the surface of Hex-HfO₂ is relatively smooth with weak scattering characteristics^[32] (Figure S12, Supporting Information).

Ru/Hex-HfO₂ was then synthesized through a two-step process. First, the synthesized Hex-HfO₂ powder was mixed with RuCl₃. The mixture was impregnated by ultrasound, followed by centrifugation and drying. Then, the products were heated to 200 °C and maintained for 2 h under an Ar/H₂ (H₂: 5%) atmosphere (Figure 2a). The final Ru/Hex-HfO₂ powder is brown and the XRD pattern shows that the Ru/Hex-HfO₂ and Hex-HfO₂ exhibit the same diffraction peaks. No diffraction peaks related to metallic Ru were detected, which may be due to the low content and high dispersion of Ru species^[33] (Figure S13a,b, Supporting Information). STEM-EDX images demonstrate that Hf, O, and Ru are uniformly distributed in 2D hexagonal nanosheets (Figure 2b). The STEM-electron energy-loss spectroscopy (STEM-EELS) line scanning profile shown in Figure S13c,d (Supporting Information) further reveals the uniform distribution of Ru. The elemental analysis and inductively coupled plasma optical emission spectrometry (ICP-OES) results indicate that the mass fraction of Ru is 3.39 (Table S1, Supporting Information). To further demonstrate the structure of Ru/Hex-HfO₂, the HRTEM image shown in Figure 2c clearly reveals that Ru nanoclusters (NCs) display a uniform and similar size of ≈1.4 nm on Hex-HfO₂ nanosheet (Figure 2d). In addition, Ru/Hex-HfO₂ with different Ru contents were also prepared and the corresponding products were denoted as Ru/Hex-HfO₂-3, Ru/Hex-HfO₂-14, Ru/Hex-HfO₂-20, and Ru/Hex-HfO₂-30. The ICP-OES shows that the measured mass fractions of Ru are 1.73, 5.11, 7.23, and 9.45, respectively (Table S1, Supporting Information). The TEM and EDX analysis images are given in Figures S14–S17 (Supporting Information). All the samples exhibit similar morphology and element distribution.

Meanwhile, to highlight the role of the hexagonal phase structure, we used the same method to synthesize Ru/M-HfO₂ for comparison. The related structure and morphology characterizations are shown in Figure S18 (Supporting Information). Due to the low atomic ratio of Ru species, the diffraction peaks of Ru were also not observed in the XRD pattern (Figure S18a, Supporting Information). TEM images clearly show that the Ru nanocrystals are loaded on the nanoparticles of M-HfO₂ (Figure S18c–e, Supporting Information). EDX images show that Hf, O, and Ru are distributed evenly throughout the nanoparticles (Figure S18h–l, Supporting Information).

The detailed element composition and electronic structures of Ru/Hex-HfO₂ were studied by XPS and XANES. As shown in Figure S19 (Supporting Information), the XPS full spectra confirmed the presence of Ru, O, and Hf elements in Ru/Hex-HfO₂. Figure 2e illustrates that the peak intensity of the white line for Ru/Hex-HfO₂ is slightly higher than that of Hex-HfO₂, indicating the valence state of Hf in Ru/Hex-HfO₂ is higher than that of Hex-HfO₂. Additionally, the Hf 4f XPS spectra of Ru/Hex-HfO₂ (Figure S20, Supporting Information) show a noticeable positive shift of Hf 4f_{7/2} and 4f_{5/2} peaks compared to Hex-HfO₂, which clearly reveals the pronounced electron transfer from Hex-HfO₂ to Ru clusters. The negative shift of Ru 3d_{5/2} peak for

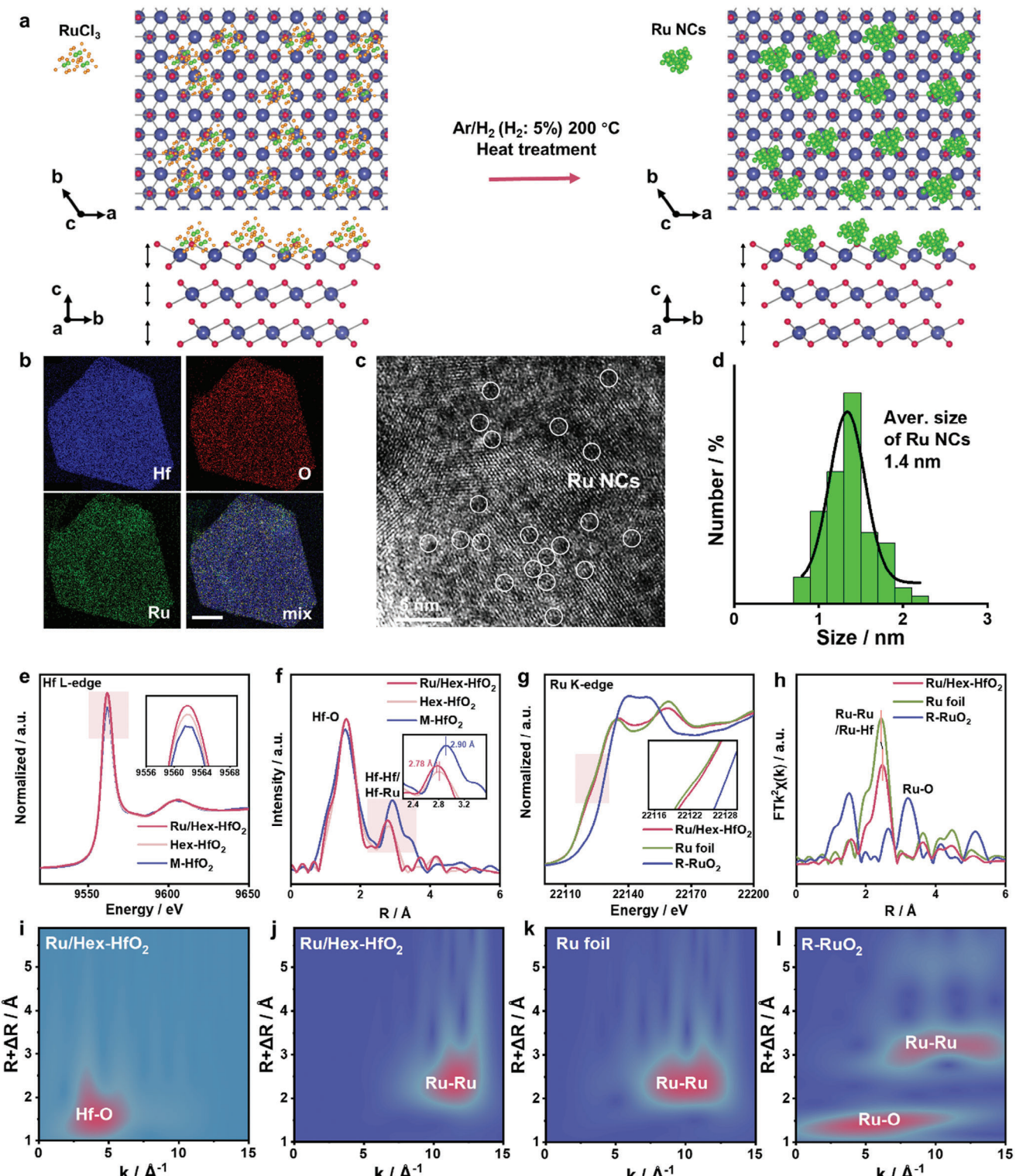


Figure 2. Morphology and electronic structure characterization. a) Schematic of the synthetic route of Ru/Hex-HfO₂. b) Elemental mapping images of Ru/Hex-HfO₂. c) HRTEM image of Ru/Hex-HfO₂. d) Particle size distribution of Ru nanoclusters (NCs) on Hex-HfO₂. e) Hf L-edge XANES spectra of Hex-HfO₂, Ru/Hex-HfO₂ and M-HfO₂. f) Fourier-transformed EXAFS spectra of Hf L-edge spectra of Hex-HfO₂, Ru/Hex-HfO₂, and M-HfO₂. g) Ru K-edge XANES spectra of Ru/Hex-HfO₂, Ru foil and rutile phase RuO₂ (R-RuO₂). h) Fourier-transformed EXAFS spectra of Ru K-edge spectra of Ru/Hex-HfO₂, Ru foil, and R-RuO₂. i) Hf L-edge WT-EXAFS of Ru/Hex-HfO₂. j-l) Ru K-edge WT-EXAFS of Ru/Hex-HfO₂, Ru foil and R-RuO₂.

Ru/Hex-HfO₂ compared with Ru/M-HfO₂ further confirms that Ru clusters obtain electrons (Figure S21, Supporting Information). The FT-EXAFS spectra of the Hf L-edge for Ru/Hex-HfO₂ closely resemble those of Hex-HfO₂, featuring a peak at 2.75 Å, which is slightly lower than the 2.78 Å observed for Hex-HfO₂. This shift indicates the presence of Hf–Hf and Hf–Ru coordination modes in the Ru/Hex-HfO₂ (Figure 2f).^[34] For the Ru K-edge XANES, the valence state of Ru of Ru/Hex-HfO₂ mainly exists in a metallic state, which is consistent with the XPS results (Figure 2g). In Ru K-edge EXAFS spectra, a dominant peak at 2.47 Å is observed in Ru/Hex-HfO₂, which further indicates the presence of metallic Ru, in agreement with the Ru K-edge XANES results^[34] (Figure 2h). The local structure of Ru/Hex-HfO₂ is further observed using the wavelet transform of EXAFS. A strong signal was observed at $\approx 4.4 \text{ \AA}^{-1}$ in k space and $\approx 1.6 \text{ \AA}$ in R space, which was attributed to the coordination contribution between Hf and O atoms (Figure 2i). Meanwhile, the results show that Ru loading does not change the coordination mode of Hex-HfO₂. The intensity maximum at 12 Å⁻¹ in k space associated with the Ru–Ru bond was detected in Ru/Hex-HfO₂, further confirming that Ru NCs were metallic state^[35] (Figure 2j–l). All structure and characterization information conclude that metallic Ru NCs are successfully coupled with the metastable-phase Hex-HfO₂.

To evaluate the HER performance of Ru/Hex-HfO₂, a typical three-electrode system in N₂-saturated 0.5 M H₂SO₄ solution was applied using a Hg/Hg₂Cl₂ electrode and a graphite rod as reference and counter electrodes, respectively. Two Pt electrodes were used as the working and counter electrodes to calibrate the Hg/Hg₂Cl₂ electrode (Figure S22, Supporting Information). For comparison, commercial Pt/C (20%), Ru/C (5%), Ru/M-HfO₂, and Hex-HfO₂ were also measured. The typical polarization curves are presented in Figure 3a and Ru/Hex-HfO₂ exhibited the best performance. In detail, Ru/Hex-HfO₂ achieved an overpotential of 8 mV at the current density of 10 mA cm⁻², which is much lower than those of Pt/C (33 mV), Ru/C (79 mV), Ru/M-HfO₂ (154 mV) and Hex-HfO₂ (369 mV) (Figure 3a,e). Moreover, Ru/Hex-HfO₂ achieved a current density of 200 mA cm⁻² at an overpotential of 293, 59, and 199 mV lower than those of Pt/C and Ru/C. The electrochemical impedance spectroscopy (EIS) curves shown in Figure S23 (Supporting Information) display a smaller charge transfer resistance (R_{ct}) of Ru/Hex-HfO₂ (43.2 ohm) than those of Pt/C (55.5 ohm) and Ru/M-HfO₂ (119.1 ohm). Figure S24 (Supporting Information) indicates that there is an optimal value of Ru content. The exchange current density ($|j_0|$) of Ru/Hex-HfO₂ is 2.11 mA cm⁻², 1.62 times higher than that of Pt/C (1.30 mA cm⁻²), indicating its outstanding HER activity (Table S2, Supporting Information). Then, the mass activity (MA) of Ru/Hex-HfO₂ at the overpotential of 30 mV is up to 14.37 A mg_{Ru}⁻¹, 33.4, 53.2 and 71.9 times higher than those of Pt/C (0.43 A mg_{Pt}⁻¹), Ru/C (0.27 A mg_{Ru}⁻¹) and Ru/M-HfO₂ (0.20 A mg_{Ru}⁻¹), respectively (Figure 3b). Meanwhile, Ru/Hex-HfO₂ exhibits an excellent MA compared with most reported Ru-based catalysts (Figure 3c,e). The corresponding Tafel slopes of Ru/Hex-HfO₂, Pt/C, Ru/C, Ru/M-HfO₂, and Hex-HfO₂ are 24, 35, 79, 145 and 387 mV dec⁻¹, respectively, indicating that Ru/Hex-HfO₂ exhibits the fastest kinetic rate toward hydrogen evolution (Figure 3d). As illustrated in Figure 3f and Tables S3 and S4 (Supporting Information), Ru/Hex-HfO₂ demonstrates

outstanding activity among the leading Ru-based electrocatalysts for the HER reported in the literature.

The electrochemical specific surface areas (ECSA) from double-layer capacitance (C_{dl}) of Ru/Hex-HfO₂, Pt/C, Ru/C, and Ru/M-HfO₂ are determined to be 30.87, 54.44, 19.31, and 13.33 cm² (Figures S25–S27, Supporting Information). The HER activity normalized to the ECSA values was also calculated (Figure 3b; Figure S26, Supporting Information). The specific activity of Ru/Hex-HfO₂ is higher than those of all the other samples, indicating that Ru/Hex-HfO₂ has superior intrinsic HER catalytic activity (Tables S5 and S6, Supporting Information).

The operational durability is the key to evaluating the application potential of HER catalysts. As shown in Figure 3g, the potential of Ru/Hex-HfO₂ exhibits limited variation after a 150 h stability test at the current density of 10 mA cm⁻². In sharp comparison, Pt/C, Ru/C, and Ru/M-HfO₂ drop 64, 240, and 550 mV under the same current density, respectively. Notably, industrial catalysts require the ability to withstand high current density. More interestingly, Ru/Hex-HfO₂ nearly shows no current loss after a 120 h operation at a constant current density of 310 mA cm⁻² (Figure 3h). The exceptional durability confirms the superior structural stability of the Ru/Hex-HfO₂ catalyst. The characterization of Ru/Hex-HfO₂ after the stability test reveals that there are negligible changes in both crystallinity and valence (Figures S28 and S29, Supporting Information). The dissolution of Ru ions in the electrolyte during the Ru/Hex-HfO₂ stability test was measured at various time points using ICP-OES analysis and the solubility of Ru ions remained consistently low (below 20.0 ppb) and exhibited only slight variations over time (Table S7, Supporting Information).

It is noteworthy that the Tafel slope of Ru/Hex-HfO₂ is only 24 mV dec⁻¹, evidently lower than the value (30 mV dec⁻¹) via the conventional Volmer–Heyrovsky/Tafel mechanism, which may imply a hydrogen spillover mechanism^[36,37] (Note S1, Supporting Information). The hydrogen spillover could be initially explored by the color change in the mixture of Ru/Hex-HfO₂ and WO₃. First, as seen in Figure S30 (Supporting Information) and Figure 4a₁,b₁, the WO₃, WO₃, and Hex-HfO₂, WO₃, and M-HfO₂ exhibit an unchanged color before and after H₂ treatment. However, the mixture of Ru/Hex-HfO₂ and WO₃ after H₂ treatment generates a dark blue color. Therefore, the schematic illustration of Figure 4a shows the color change process of WO₃, the spilled-over H migrates and readily reacts with WO₃ to form dark blue H_xWO₃.^[38] Notably, the mixture of Ru/M-HfO₂ and WO₃ does not change color after H₂ treatment (Figure 4b,b₁). This indicates that the metastable-phase substrate plays a crucial role in the process of hydrogen spillover.

Hydrogen temperature-programmed desorption (H₂-TPD) can also monitor the presence of spilled H species by desorbing hydrogen.^[39] This is because hydrogen spillover in electrocatalysis involves the migration of active hydrogen (H^{*}) from a metal with strong hydrogen adsorption to a substrate with weak hydrogen adsorption, thereby facilitating hydrogen desorption. Therefore, the decrease in the desorption peak temperature of H indicates a weaker hydrogen adsorption strength, thereby confirming the presence of hydrogen spillover.^[40] As shown in Figure 4g, H₂-TPD profiles showed that no H₂ desorption peak was observed for Hex-HfO₂. After Ru loading, a new H₂ desorption peak occurs between 341 and 425 °C for Ru/M-HfO₂. When Ru was deposited

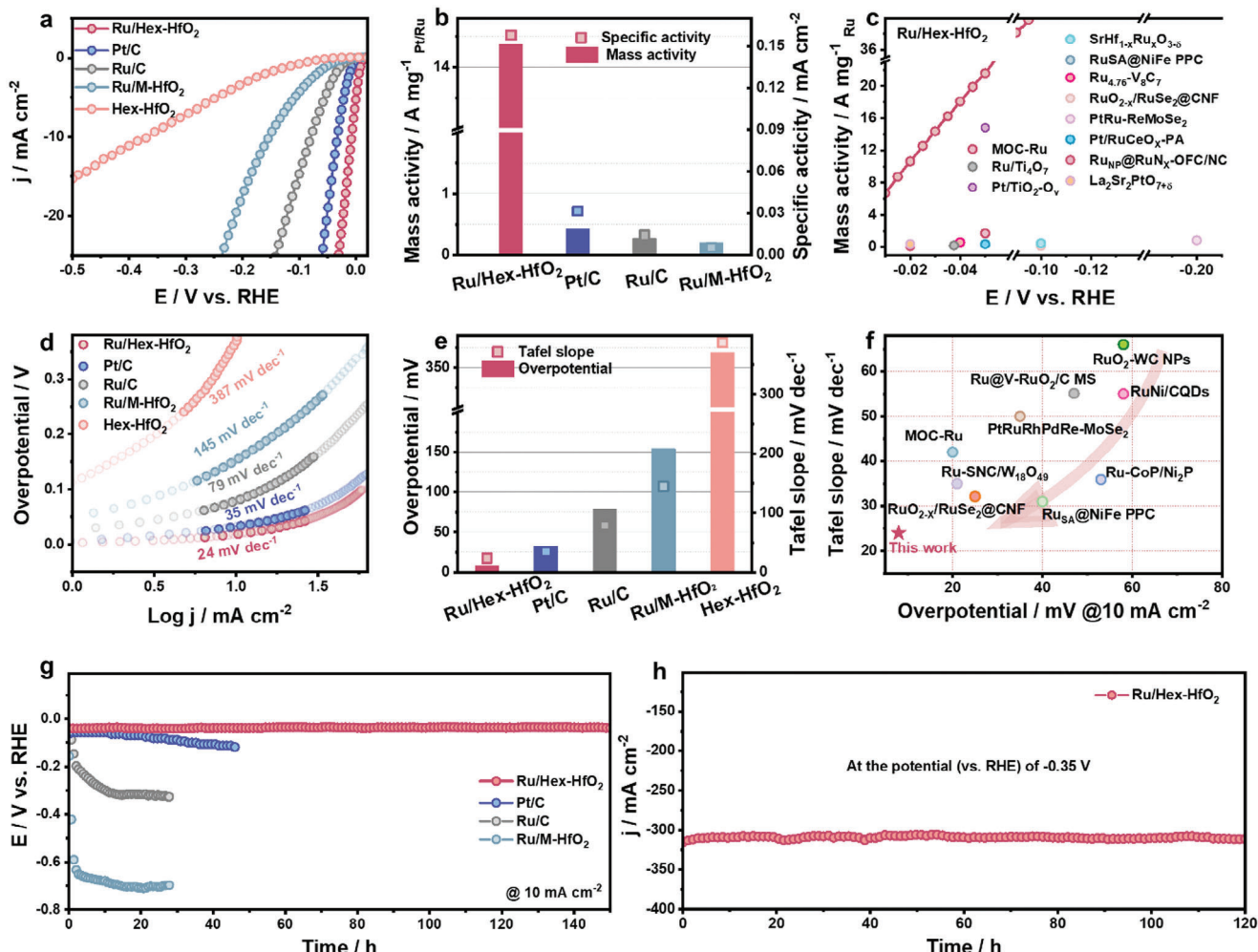


Figure 3. HER performance of Ru/Hex-HfO₂ electrocatalysts and the reference samples in 0.5 M H₂SO₄. a) The HER polarization curves of Ru/Hex-HfO₂, Pt/C, Ru/C, Ru/M-HfO₂ and Hex-HfO₂. b) The comparison of mass activities and specific activities for different catalysts at the overpotential of 30 mV. c) Mass activity curve and comparison with reported Ru-based catalysts.^[5,48–57] d) Tafel plots of Ru/Hex-HfO₂, Pt/C, Ru/C, Ru/M-HfO₂ and Hex-HfO₂. e) The comparison of overpotentials at 10 mA cm⁻² and Tafel slope for different catalysts. f) The comparison of the Tafel slope and overpotential of Ru/Hex-HfO₂ and reported Ru-based catalysts.^[3,54–61] g) Stability of Ru/Hex-HfO₂, Pt/C, Ru/C, and Ru/M-HfO₂ by chronopotentiometry technique at a constant current density of -10 mA cm^{-2} . h) The stability test for Ru/Hex-HfO₂ by chronoamperometry test under the potential (vs RHE) of -0.35 V for 120 h.

on a Hex-HfO₂ substrate, the H₂ desorption peak downshifted to 278 °C, which ascribed to the lower H adsorption energy in Ru/Hex-HfO₂ compared to Ru/M-HfO₂. This change provides strong evidence for the effective spillover of dissociated hydrogen atoms from Ru clusters onto the Hex-HfO₂ substrate surface, validly supporting the HSPE concept.

Besides, the hydrogen spillover effect could also be verified by electrochemical experiments. The reaction mechanism of HER was substantiated by pH-dependent experiments. As shown in Figures 4c and S31 (Supporting Information), the reaction order of 1.98 for Ru/Hex-HfO₂ is in close alignment with the theoretical value of 2, which means that the rate of reaction is proportional to the square of H⁺ concentration.^[36] It shows that there are two H⁺ ions involved in the rate-determining step, while Ru/M-HfO₂ only exhibits a significantly low reaction order of 0.42. Furthermore, conducting the in situ analysis of the hy-

drogen adsorption and desorption kinetics on catalysts can provide supporting evidence for the occurrence of hydrogen spillover since the hydrogen spillover effect can effectively accelerate the hydrogen desorption kinetics of electrocatalysts. To investigate the kinetics of hydrogen desorption, the hydrogen desorption peaks in the double layer region were monitored during CV scanning^[41] (Figure 4d; Figures S32 and S33, Supporting Information). The CV curves of Ru/Hex-HfO₂ and Ru/M-HfO₂ demonstrate a shift in the hydrogen desorption peak depending on the scanning rate. As shown in Figure 4e, the slope follows the order of Ru/Hex-HfO₂ < Ru/M-HfO₂. The significantly reduced slope for Ru/Hex-HfO₂ suggests its accelerated hydrogen desorption kinetics. Kinetic isotope effects (KIEs) involving H and deuterium (D) reflect the alterations in reaction rates arising from their mass differences. When the KIEs value exceeds 1.5, it suggests that significant hydrogen or proton transfer occurs

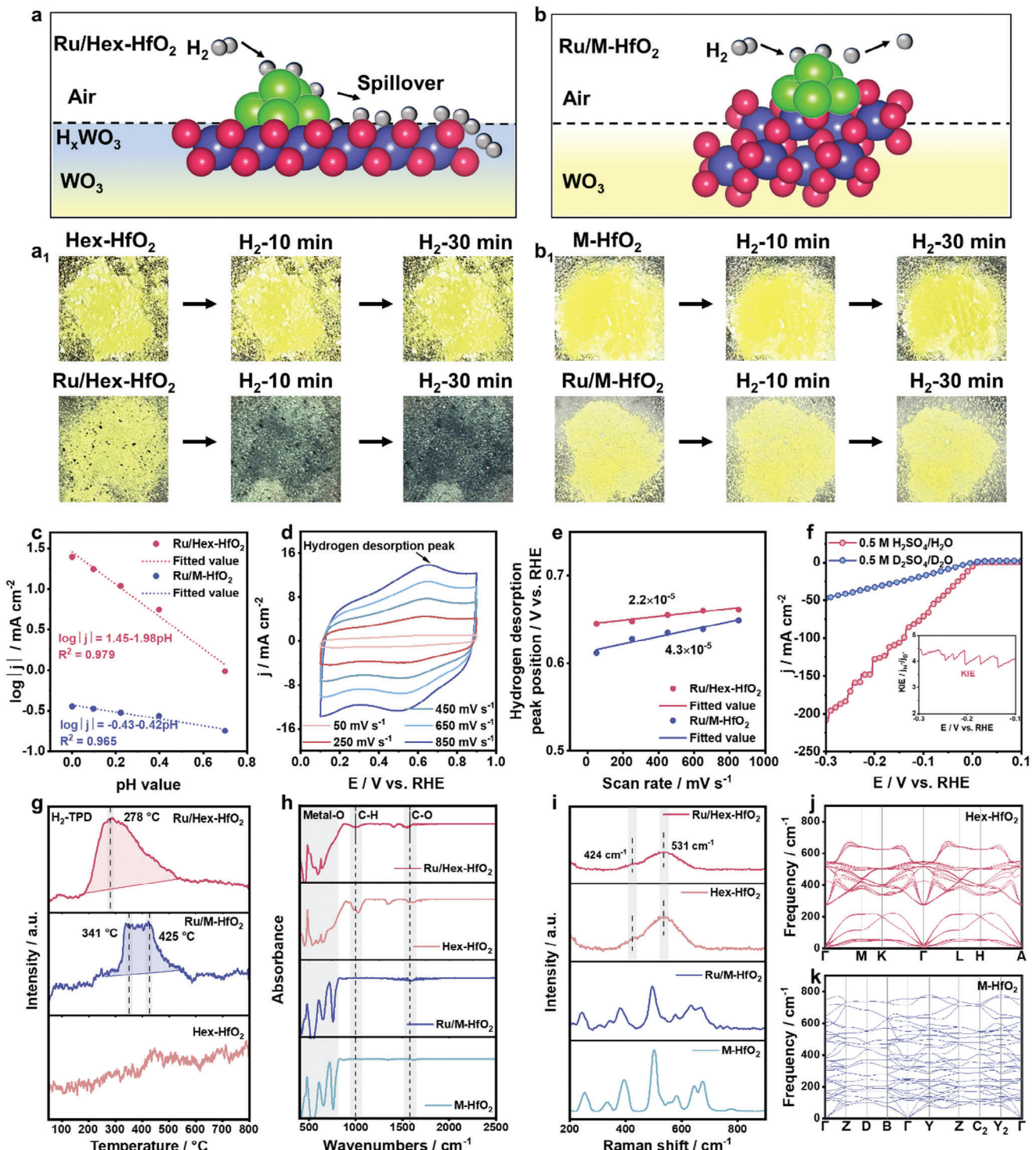


Figure 4. Experimental evidence for hydrogen spillover. Schematic illustration of the color change of a) Ru/Hex-HfO₂ and WO₃ and b) Ru/M-HfO₂ and WO₃. a₁) The photographic image of the physical mixture for Hex-HfO₂ and WO₃, Ru/Hex-HfO₂ and WO₃ before H₂ treatment and after H₂ treatment for 10 min and 30 min at room temperature. b₁) The photographic image of the physical mixture for M-HfO₂ and WO₃, Ru/M-HfO₂ and WO₃ before H₂ treatment and after H₂ treatment for 10 and 30 min at room temperature. c) The liner plot of $\log|j|$ at -0.03 V (vs RHE) versus pH of Ru/Hex-HfO₂ and Ru/M-HfO₂. d) CV profiles of Ru/Hex-HfO₂ with the scan rate from 50 to 850 mV s⁻¹ in Ar-saturated 0.5 M H₂SO₄. e) Plots of hydrogen desorption peak position versus scan rates of Ru/Hex-HfO₂ and Ru/M-HfO₂. f) Polarization curves of Ru/Hex-HfO₂ in 0.5 M H₂SO₄ and 0.5 M D₂SO₄ solutions. The inset is the kinetic isotope effect value versus potential. g) H₂-TPD profiles of Ru/Hex-HfO₂, Ru/M-HfO₂ and Hex-HfO₂. h) FTIR spectra of Ru/Hex-HfO₂, Ru/M-HfO₂, Hex-HfO₂ and M-HfO₂. i) Raman spectra of Ru/Hex-HfO₂, Ru/M-HfO₂, Hex-HfO₂ and M-HfO₂. The Brillouin phonon spectra of j) Hex-HfO₂ and k) M-HfO₂.

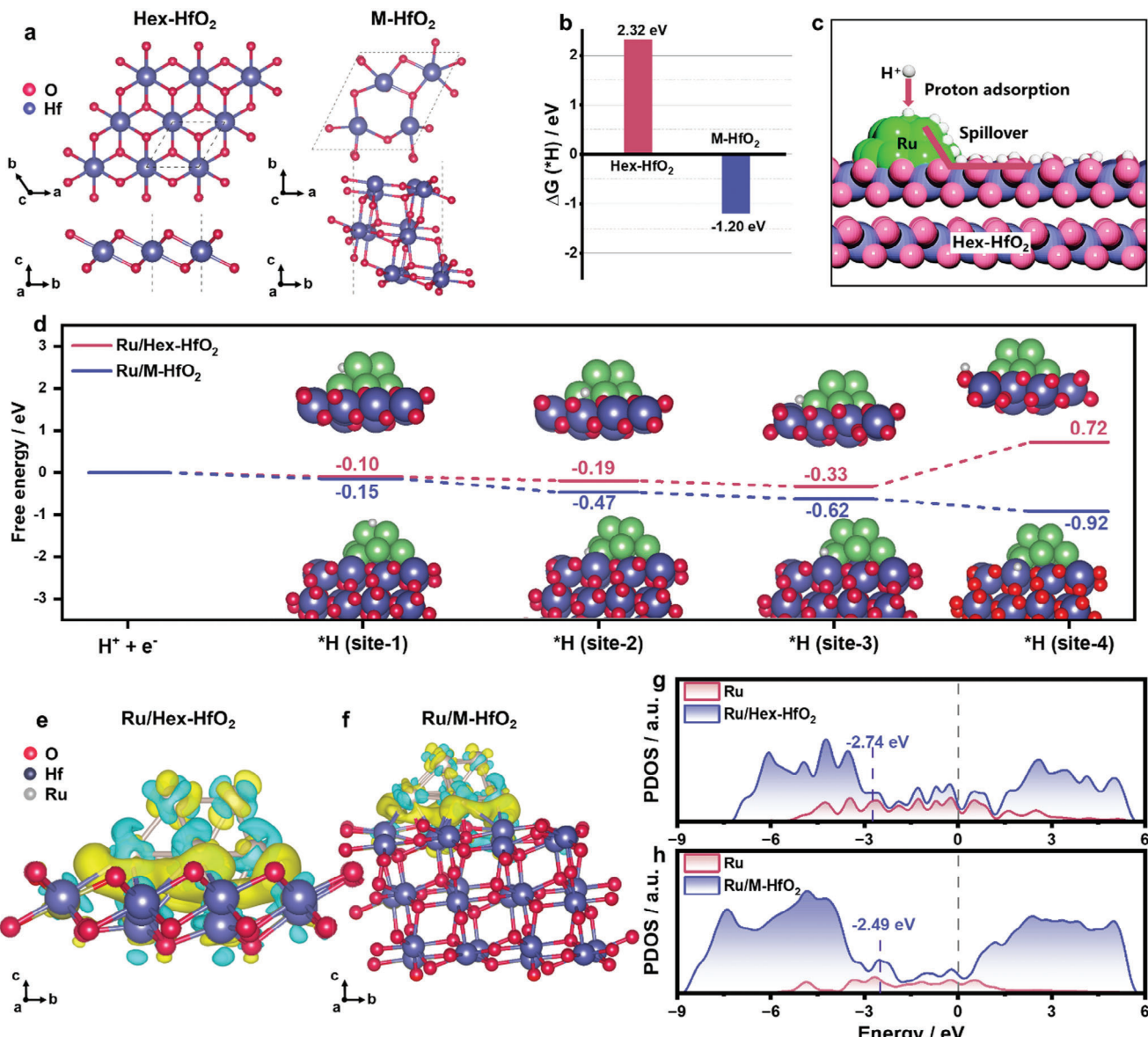


Figure 5. DFT calculations. a) Top and side views of pristine Hex-HfO₂ and M-HfO₂. b) Comparison of hydrogen adsorption-free energies on pristine Hex-HfO₂ and M-HfO₂. c) Schematic illustration of hydrogen spillover on Ru/Hex-HfO₂. d) Gibbs free energy of hydrogen spillover of Ru/Hex-HfO₂ and Ru/M-HfO₂ and the corresponding adsorption configurations. Charge density difference plots of e) Ru/Hex-HfO₂ and f) Ru/M-HfO₂. The isosurface values of 0.005 e Å⁻³ were set. Projected Density of States (PDOS) plots of g) Ru/Hex-HfO₂ and h) Ru/M-HfO₂.

during the reaction.^[42–44] The polarization curve of Ru/Hex-HfO₂ in 0.5 M D₂SO₄/D₂O electrolyte exhibits a significantly lower current density in comparison with that in the 0.5 M H₂SO₄/H₂O electrolyte over the entire potential range (Figure 4f). The KIE value of Ru/Hex-HfO₂ exceeding 3.5 suggests that hydrogen or proton transfer could be a rate-limiting step in the reaction.

Furthermore, we elucidated the active sites of Ru/Hex-HfO₂ in HER by introducing thiocyanate ions (SCN[−]) or tetramethylammonium cations (TMA⁺), which have specific interactions with the metal and oxygen-containing species, respectively.^[45] As shown in Figure S34 (Supporting Information), the addition of these chemical probes resulted in the significant performance deterioration of Ru/Hex-HfO₂, respectively, indicating that both

Ru and Hex-HfO₂ play important roles in HER. However, Ru/M-HfO₂ exhibits significant performance degradation upon the addition of SCN[−], while there is almost no decline in performance with the addition of TMA⁺, indicating that Ru is the sole active site in Ru/M-HfO₂. The HER performance of Hex-HfO₂ decreased significantly only after the addition of TMA⁺, indicating that the oxide is the main active site of HER. Specifically, the Ru/C exhibited pronounced performance loss when adding SCN[−], while the performance remained largely unaffected upon TMA⁺ addition, suggesting that the metal Ru in Ru/C is the sole active site and TMA⁺ has no impact on Ru.

The chemical bonds and molecular vibrations in Hex-HfO₂ were demonstrated by Fourier transform infrared spectroscopy

(FTIR) and Raman spectroscopy. In the FTIR spectra, the different absorption peaks in the range of 400–800 cm⁻¹ indicate that there are distinctly different metal-oxygen bond vibrations in Hex-HfO₂ and M-HfO₂ (Figure 4h). Furthermore, the absence of imaginary frequencies in the phonon spectrum confirms the dynamic stability of the new Hex-HfO₂ phase (Figure 4j). Based on the phonon spectra, we analyzed the Raman active modes for both the Hex-HfO₂ and M-HfO₂ phases. Hex-HfO₂ exhibits 24 Raman-active modes with $\Gamma_{\text{raman}} = 8A_1 + 9E_2 + 8F_1$, showing strong correspondence with the experimental Raman scattering spectra (Figure 4i). The mode at ≈ 531 cm⁻¹ (the prominent peak in the experiment) corresponds to an A₁ mode, which relates to the collective translational vibration of the O atoms along the c-axis (Figure S35a, Supporting Information). The phonon mode at 424 cm⁻¹, corresponding to the shoulder peak at ≈ 424 cm⁻¹ in experimental Raman, is attributed to the interlayer stretching vibration of the O atoms along the c-axis (Figure S35b and Tables S8 and S9, Supporting Information).

DFT calculations were performed to gain insights into the enhanced HER performance on Ru/Hex-HfO₂. At first, we chose the Hex-HfO₂ (001) surface and M-HfO₂ (-111) surface to support the Ru₁₀ cluster as the representative theoretical models of Ru/Hex-HfO₂ and Ru/M-HfO₂ for HER (Figure 5a; Note S2, Supporting Information). Then we systematically investigated the hydrogen adsorption on pristine Hex-HfO₂ and M-HfO₂ and found that, for Hex-HfO₂, the proton is prone to adsorb on the surface O with the H adsorption Gibbs free energies (ΔG_H) of 2.32 eV, while for M-HfO₂, the proton is more likely to adsorb at the Hf–Hf bridge site with a ΔG_H of -1.20 eV (Figure 5b). A negative ΔG_H value corresponds to unfavorable hydrogen desorption on M-HfO₂, while a positive ΔG_H value on Hex-HfO₂ is helpful for the H spillover, where the H is captured by the Ru cluster to form the adsorbed H, then migrates from Ru to Hex-HfO₂ and desorbs on Hex-HfO₂ (Figure 5c). Figure 5d presents the energy evolution diagram of hydrogen spillover from the Ru cluster to the HfO₂ substrate. For Ru/Hex-HfO₂, the H adsorption prefers to occur at Ru sites with a negative ΔG_H value of -0.10 eV (Ru-top, site-1), -0.19 eV (Ru–Ru bridge, site-2) and -0.33 eV (Ru–Hf bridge, site-3), whereas the Hex-HfO₂ substrate (site-4) exhibits a positive ΔG_H value of 0.72 eV, which facilitates the desorption of hydrogen intermediate during HER. In contrast, for Ru/M-HfO₂, the ΔG_H values are -0.15 eV (Ru-top, site-1), -0.47 eV (Ru–Ru bridge, site-2), -0.62 eV (Ru–Hf bridge, site-3) and -0.92 eV (Hf–HfO₂ substrate, site-4), showing a progressively enhanced proton adsorption. These differences can be attributed to the distinct atomic environment of Hf atoms on the Hex-HfO₂ and M-HfO₂ surfaces. In Hex-HfO₂, the Hf atoms are fully coordinated with oxygen. Conversely, the proton prefers to attack the exposed Hf sites of M-HfO₂, promoting its adsorption. Electronic property analysis reveals that after the loading of the Ru cluster on Hex-HfO₂ and M-HfO₂, there exists electron transfer from the HfO₂ support to the Ru cluster (Figure 5e,f). By quantitative Bader charge analysis, the Ru cluster gains 4.92 e from the support Hex-HfO₂, more than that (3.07 e) from M-HfO₂. The charge transfer from HfO₂ to Ru further shifts the d-band center for Ru in Ru/Hex-HfO₂ (-2.74 eV) farther away from the Fermi energy level compared with that of Ru/M-HfO₂ (-2.49 eV) (Figure 5g,h). The downshift of the d-band center usually weakens the hydrogen adsorption,^[46,47] thus promoting the hydrogen

spillover. Therefore, our DFT calculations confirm that the interaction between Ru clusters and Hex-HfO₂ enables the optimized hydrogen adsorption and facilitates the surface H spillover, which is consistent with the electrocatalytic performance we obtained experimentally.

3. Conclusion

In summary, we first discovered that metastable-phase substrate engineering can effectively trigger the hydrogen spillover effect. We successfully synthesized metastable hexagonal phase hafnium oxide (Hex-HfO₂, space group: P6₃mc (186)) and observed significant hydrogen spillover when loading with Ru, while it does not occur on the monoclinic phase hafnium oxide (M-HfO₂, space group: P2₁/c (14)). Thanks to the generated hydrogen spillover, Ru/Hex-HfO₂ has high mass activity of 14.37 A mg_{Ru}⁻¹ at the overpotential of 30 mV. This work provides insights into hydrogen spillover triggered by metastable-phase substrate toward various energy applications.

Supporting Information

Supporting Information is available from the Wiley Online Library or from the author.

Acknowledgements

This work was financially supported by the Ministry of Science and Technology of China (2024YFA1509500), National Natural Science Foundation of China (22475143), Young Elite Scientists Sponsorship Program by CAST (grant no. 2023QNRC001), the Priority Academic Program Development of Jiangsu Higher Education Institutions (PAPD) and Collaborative Innovation Center of Suzhou Nano Science and Technology.

Conflict of Interest

The authors declare no conflict of interest.

Data Availability Statement

The data that support the findings of this study are available from the corresponding author upon reasonable request.

Keywords

hydrogen spillover, metastable-phase, six-hexagonal phase hafnium dioxide

Received: October 19, 2024

Revised: February 18, 2025

Published online:

[1] B. Y. Tang, R. P. Bisbey, K. M. Lodaya, W. L. Toh, Y. Surendranath, *Nat. Catal.* **2023**, *6*, 339.

- [2] P. Li, Y. Jiang, Y. Hu, Y. Men, Y. Liu, W. Cai, S. Chen, *Nat. Catal.* **2022**, 5, 900.
- [3] Y. Pi, Z. Qiu, Y. Sun, H. Ishii, Y.-F. Liao, X. Zhang, H.-Y. Chen, H. Pang, *Adv. Sci.* **2023**, 10, 2206096.
- [4] F. Li, G.-F. Han, H.-J. Noh, J.-P. Jeon, I. Ahmad, S. Chen, C. Yang, Y. Bu, Z. Fu, Y. Lu, J.-B. Baek, *Nat. Commun.* **2019**, 10, 4060.
- [5] J. Dai, Y. Zhu, Y. Chen, X. Wen, M. Long, X. Wu, Z. Hu, D. Guan, X. Wang, C. Zhou, Q. Lin, Y. Sun, S.-C. Weng, H. Wang, W. Zhou, Z. Shao, *Nat. Commun.* **2022**, 13, 1189.
- [6] Z. Zhang, Z. Zhang, C. Chen, R. Wang, M. Xie, S. Wan, R. Zhang, L. Cong, H. Lu, Y. Han, W. Xing, Z. Shi, S. Feng, *Nat. Commun.* **2024**, 15, 2556.
- [7] O. Bünermann, H. Jiang, Y. Dorenkamp, A. Kandratsenka, S. M. Janke, D. J. Auerbach, A. M. Wodtke, *Science* **2015**, 350, 1346.
- [8] J. Cai, Y. Song, Y. Zang, S. Niu, Y. Wu, Y. Xie, X. Zheng, Y. Liu, Y. Lin, X. Liu, G. Wang, Y. Qian, *Sci. Adv.* **2020**, 6, eaaw8113.
- [9] F. Zaera, *Nature* **2017**, 541, 37.
- [10] H. Kang, L. Zhu, S. Li, S. Yu, Y. Niu, B. Zhang, W. Chu, X. Liu, S. Perathoner, G. Centi, Y. Liu, *Nat. Catal.* **2023**, 6, 1062.
- [11] A. Mahdavi-Shakib, T. N. Whittaker, T. Y. Yun, K. B. Sravan Kumar, L. C. Rich, S. Wang, R. M. Rioux, L. C. Grabow, B. D. Chandler, *Nat. Catal.* **2023**, 6, 710.
- [12] X.-J. Bai, C. Yang, Z. Tang, *Nat. Commun.* **2024**, 15, 6263.
- [13] L. Jiang, K. Liu, S.-F. Hung, L. Zhou, R. Qin, Q. Zhang, P. Liu, L. Gu, H. M. Chen, G. Fu, N. Zheng, *Nat. Nanotechnol.* **2020**, 15, 848.
- [14] S. Wu, K.-Y. Tseng, R. Kato, T.-S. Wu, A. Large, Y.-K. Peng, W. Xiang, H. Fang, J. Mo, I. Wilkinson, Y.-L. Soo, G. Held, K. Suenaga, T. Li, H.-Y. T. Chen, S. C. E. Tsang, *J. Am. Chem. Soc.* **2021**, 143, 9105.
- [15] G. Zhan, H. C. Zeng, *Nat. Commun.* **2018**, 9, 3778.
- [16] M. Tan, Y. Yang, Y. Yang, J. Chen, Z. Zhang, G. Fu, J. Lin, S. Wan, S. Wang, Y. Wang, *Nat. Commun.* **2022**, 13, 1457.
- [17] K. Shun, K. Mori, T. Kidawara, S. Ichikawa, H. Yamashita, *Nat. Commun.* **2024**, 15, 6403.
- [18] J. Li, J. Hu, M. Zhang, W. Gou, S. Zhang, Z. Chen, Y. Qu, Y. Ma, *Nat. Commun.* **2021**, 12, 3502.
- [19] W. Karim, C. Spreafico, A. Kleibert, J. Gobrecht, J. VandeVondele, Y. Ekinci, J. A. van Bokhoven, *Nature* **2017**, 541, 68.
- [20] J. Li, Y. Ma, J. C. Ho, Y. Qu, *Acc. Chem. Res.* **2024**, 57, 895.
- [21] Z. Fan, F. Liao, Y. Ji, Y. Liu, H. Huang, D. Wang, K. Yin, H. Yang, M. Ma, W. Zhu, M. Wang, Z. Kang, Y. Li, M. Shao, Z. Hu, Q. Shao, *Nat. Commun.* **2022**, 13, 5828.
- [22] Q. Dang, H. Lin, Z. Fan, L. Ma, Q. Shao, Y. Ji, F. Zheng, S. Geng, S.-Z. Yang, N. Kong, W. Zhu, Y. Li, F. Liao, X. Huang, M. Shao, *Nat. Commun.* **2021**, 12, 6007.
- [23] F. Liao, K. Yin, Y. Ji, W. Zhu, Z. Fan, Y. Li, J. Zhong, M. Shao, Z. Kang, Q. Shao, *Nat. Commun.* **2023**, 14, 1248.
- [24] W. Zhu, X. Song, F. Liao, H. Huang, Q. Shao, K. Feng, Y. Zhou, M. Ma, J. Wu, H. Yang, H. Yang, M. Wang, J. Shi, J. Zhong, T. Cheng, M. Shao, Y. Liu, Z. Kang, *Nat. Commun.* **2023**, 14, 5365.
- [25] Z. Fan, Y. Ji, Q. Shao, S. Geng, W. Zhu, Y. Liu, F. Liao, Z. Hu, Y.-C. Chang, C.-W. Pao, Y. Li, Z. Kang, M. Shao, *Joule* **2021**, 5, 3221.
- [26] U. Schroeder, M. H. Park, T. Mikolajick, C. S. Hwang, *Nat. Rev. Mater.* **2022**, 7, 653.
- [27] H. Yang, Y. Ji, Q. Shao, W. Zhu, M. Fang, M. Ma, F. Liao, H. Huang, Y. Zhang, J. Yang, Z. Fan, Y. Li, Y. Liu, M. Shao, Z. Kang, *Energy Environ. Sci.* **2023**, 16, 574.
- [28] G. Li, H. Jang, S. Liu, Z. Li, M. G. Kim, Q. Qin, X. Liu, J. Cho, *Nat. Commun.* **2022**, 13, 1270.
- [29] M. Wang, L. Árnadóttir, Z. J. Xu, Z. Feng, *Nano Micro Lett.* **2019**, 11, 47.
- [30] P. A. O'Day, J. J. Rehr, S. I. Zabinsky, G. E. Brown, Jr., *J. Am. Chem. Soc.* **1994**, 116, 2938.
- [31] A. I. Frenkel, *Chem. Soc. Rev.* **2012**, 41, 8163.
- [32] J. J. Rehr, R. C. Albers, *Rev. Mod. Phys.* **2000**, 72, 621.
- [33] J. Zhang, G. Chen, Q. Liu, C. Fan, D. Sun, Y. Tang, H. Sun, X. Feng, *Angew. Chem., Int. Ed.* **2022**, 61, 202209486.
- [34] J. Li, C. Hou, C. Chen, W. Ma, Q. Li, L. Hu, X. Lv, J. Dang, *ACS Nano* **2023**, 17, 10947.
- [35] Q. Liang, Q. Li, L. Xie, H. Zeng, S. Zhou, Y. Huang, M. Yan, X. Zhang, T. Liu, J. Zeng, K. Liang, O. Terasaki, D. Zhao, L. Jiang, B. Kong, *ACS Nano* **2022**, 16, 7993.
- [36] L. Zhu, H. Lin, Y. Li, F. Liao, Y. Lifshitz, M. Sheng, S.-T. Lee, M. Shao, *Nat. Commun.* **2016**, 7, 12272.
- [37] M. Sheng, B. Jiang, B. Wu, F. Liao, X. Fan, H. Lin, Y. Li, Y. Lifshitz, S.-T. Lee, M. Shao, *ACS Nano* **2019**, 13, 2786.
- [38] M. Xiong, Z. Gao, P. Zhao, G. Wang, W. Yan, S. Xing, P. Wang, J. Ma, Z. Jiang, X. Liu, J. Ma, J. Xu, Y. Qin, *Nat. Commun.* **2020**, 11, 4773.
- [39] H. Shen, H. Li, Z. Yang, C. Li, *Green Energy Environ.* **2022**, 7, 1161.
- [40] G. Kyriakou, M. B. Boucher, A. D. Jewell, E. A. Lewis, T. J. Lawton, A. E. Baber, H. L. Tierney, M. Flytzani-Stephanopoulos, E. C. H. Sykes, *Science* **2012**, 335, 1209.
- [41] D. Zhan, J. Velmurugan, M. V. Mirkin, *J. Am. Chem. Soc.* **2009**, 131, 14756.
- [42] W. Li, F. Li, H. Yang, X. Wu, P. Zhang, Y. Shan, L. Sun, *Nat. Commun.* **2019**, 10, 5074.
- [43] M. K. Coggins, M.-T. Zhang, Z. Chen, N. Song, T. J. Meyer, *Angew. Chem., Int. Ed.* **2014**, 53, 12226.
- [44] A. Lewandowska-Andralojc, D. C. Grills, J. Zhang, R. M. Bullock, A. Miyazawa, Y. Kawanishi, E. Fujita, *J. Am. Chem. Soc.* **2014**, 136, 3572.
- [45] Z.-F. Huang, J. Song, Y. Du, S. Xi, S. Dou, J. M. V. Nsanzimana, C. Wang, Z. J. Xu, X. Wang, *Nat. Energy* **2019**, 4, 329.
- [46] L. Tao, K. Wang, F. Lv, H. Mi, F. Lin, H. Luo, H. Guo, Q. Zhang, L. Gu, M. Luo, S. Guo, *Nat. Commun.* **2023**, 14, 6893.
- [47] Y. Zhang, Y. Zhang, B. Tian, H. Li, Z. Zeng, D. Ho, *Mater. Today Energy* **2022**, 29, 101133.
- [48] T. Liu, W. Gao, Q. Wang, M. Dou, Z. Zhang, F. Wang, *Angew. Chem., Int. Ed.* **2020**, 59, 20423.
- [49] S. Zhao, S.-F. Hung, L. Deng, W.-J. Zeng, T. Xiao, S. Li, C.-H. Kuo, H.-Y. Chen, F. Hu, S. Peng, *Nat. Commun.* **2024**, 15, 2728.
- [50] Z. Wu, P. Yang, Q. Li, W. Xiao, Z. Li, G. Xu, F. Liu, B. Jia, T. Ma, S. Feng, L. Wang, *Angew. Chem., Int. Ed.* **2023**, 62, 202300406.
- [51] Y. Wang, Q. Lu, F. Li, D. Guan, Y. Bu, *Adv. Func. Mater.* **2023**, 33, 2213523.
- [52] Y. Feng, W. Feng, J. Wan, J. Chen, H. Wang, S. Li, T. Luo, Y. Hu, C. Yuan, L. Cao, L. Feng, J. Li, R. Wen, J. Huang, *Appl. Catal. B: Environ. Energy* **2022**, 307, 121193.
- [53] Y. Long, Y. Shen, P. Jiang, H. Su, J. Xian, Y. Sun, J. Yang, H. Song, Q. Liu, G. Li, *Sci. Bull.* **2024**, 69, 763.
- [54] Y. Chen, Y. Liu, L. Li, T. Sakthive, Z. Guo, Z. Dai, *Adv. Funct. Mater.* **2024**, 34, 2406587.
- [55] Z. Luo, Y. Guo, C. He, Y. Guan, L. Zhang, Y. Li, Q. Zhang, C. He, X. Sun, X. Ren, *Angew. Chem., Int. Ed.* **2024**, 63, 202405017.
- [56] C. Yang, Z. Wu, Z. Zhao, Y. Gao, T. Ma, X. Luo, C. Cheng, Y. Wang, S. Li, C. Zhao, *Adv. Mater.* **2023**, 35, 2303331.
- [57] Z. Kou, Y. Liu, W. Cui, B. Yang, Z. Li, R. D. Rodriguez, Q. Zhang, C.-L. Dong, X. Sang, L. Lei, T. Zhang, Y. Hou, *Energy Environ. Sci.* **2024**, 17, 1540.
- [58] S. Sun, H. Jiang, Z. Chen, Q. Chen, M. Ma, L. Zhen, B. Song, C. Xu, *Angew. Chem., Int. Ed.* **2022**, 61, 202202519.
- [59] Y. Li, W. Wang, M. Cheng, Y. Feng, X. Han, Q. Qian, Y. Zhu, G. Zhang, *Adv. Mater.* **2023**, 35, 2206351.
- [60] Y. Liu, X. Li, Q. Zhang, W. Li, Y. Xie, H. Liu, L. Shang, Z. Liu, Z. Chen, L. Gu, Z. Tang, T. Zhang, S. Lu, *Angew. Chem., Int. Ed.* **2020**, 59, 1718.
- [61] H. Zhang, W. Liu, Z. Li, L. Qiao, K. Chi, X. Guo, D. Cao, D. Cheng, *Adv. Sci.* **2024**, 11, 2401398.